Robust type-II band alignment in Janus-MoSSe bilayer with extremely long carrier lifetime induced by the intrinsic electric field

Chen Long and Ying Dai*
School of Physics, State Key Laboratory of Crystal Materials, Shandong University, Jinan 250100, China

Zhi-Rui Gong and Hao Jin†
Shenzhen Key Laboratory of Advanced Thin Films and Applications, College of Physics and Optoelectronic Engineering, Shenzhen University, Shenzhen 518060, China

(Received 28 December 2018; published 26 March 2019)

van der Waals (vdW) bilayers have many attractive novel properties that offer an ideal platform for various electronic and optoelectronic applications. However, due to the strong interlayer overlapping, the electron-hole recombination lifetime in vdW bilayers is usually very short, which limits their applications. Here, based on the time-dependent density functional theory combined with nonadiabatic molecular dynamics, we demonstrate that the Janus-MoSSe bilayer can have a staggered band gap, in which the maximum valence and minimum conduction bands are spatially separated on different layers. Such type-II band alignment is surprisingly robust against external perturbations, such as twisting or stacking modes, which can be ascribed to the intrinsic out-of-plane electric field. Further analysis indicates that due to the existence of such a built-in electric field, the overlapping within the interlayer is suppressed, leading to the completely spacial detachment of the electrons and holes. We then evaluate the photogenerated electron and hole recombination dynamics. The predicted recombination time is extremely long, with a value up to 16.5 ns, which is even longer than that of the MoS_2/WS_2 vdW heterostructure. Our findings propose that introducing an intrinsic electric field is an efficient way to tune the electronic structures of bilayers, which can significantly extend the recombination time of a photoexcited electron and hole, and thus facilitate the design of advanced two-dimensional semiconducting devices.

DOI: 10.1103/PhysRevB.99.115316

I. INTRODUCTION

Following the exfoliation of graphene [1–3], two-dimensional (2D) materials that display interesting electronic and optical properties have received an extensive amount of attention [4–12]. The creation of van der Waals (vdW) heterostructures by assembling different 2D layered crystals, such as graphene, transition-metal dichalcogenides (TMDs), group III-VI layered semiconductors, and hexagonal boron nitride (h-BN), can integrate highly disparate materials at the atomic scale [13–16]. The heterostructures can be of type I, type II, or type III, depending on the relative band alignment of the valence-band maximum (VBM) and the conduction-band minimum (CBM) of the two layers. In type-II band alignment, VBM and CBM belong to independent components possessing different work functions, resulting in an efficiently spatial separation of photoexcited charge carriers. As a result, it usually leads to a long photogenerated carrier lifetime and tunable interlayer coupling [17–21]. These novel characters offer a variable platform of various electronic, optoelectronic, and valleytronic applications.

In a general way, a type-II band alignment is usually missing in a vdW bilayer due to the strong interlayer coupling, which restricts its widespread applications [22–24]. Recently, a Janus-MoSSe monolayer has been successfully synthesized by fully replacing the top layer of S atoms with Se atoms in MoS_2 [25]. The breaking of structural symmetry and the distinction of electronegativity between S and Se atoms induce an intrinsic out-of-plane electric field [26,27]. Due to the spontaneous polarization, the Janus-MoSSe monolayer exhibits many novel properties, such as a large Rashba effect, out-of-plane piezoelectricity, and spacial isolation of charge carriers [28–32].

Here, we demonstrate that with the help of the intrinsic electric field, the Janus-MoSSe vdW bilayer has a robust type-II band alignment, which remains unchanged when we alter the stacking order of the bilayer or twist the top layer to form a moiré superlattice. The robustness against external perturbation suggests that the interlayer coupling in bilayer Janus-MoSSe is suppressed, which may allow the existence of a long-lived exciton and result in an extremely low recombination rate. Using time-dependent density functional theory (TD-DFT) simulations, the deduction is further confirmed. A slow electron-hole recombination process is observed in the Janus-MoSSe bilayer, with a lifetime up to 16.5 ns, which is even larger than that of MoS_2/WS_2, MoS_2/TiO_2, and MoS_2/WSe_2 vdW heterostructures [33–35]. Our work provides a possible approach to engineering the electronic and optical properties in a vdW bilayer for potential electronic and optoelectronic applications.

*daiy60@sdu.edu.cn
†jh@szu.edu.cn

II. COMPUTATIONAL METHODOLOGY

For our first-principles calculations, we employ the plane-wave basis projector augmented wave (PAW) method [36,37] as implemented in Vienna *ab initio* Simulation Package (VASP) [38,39]. The generalized gradient approximation (GGA) in the Perdew-Burke-Ernzerhof (PBE) [40] form for the exchange and correlation potential with a plane-wave cutoff of 450 eV and an $18 \times 18 \times 1$ k-point mesh are used. The vdW correction to the GGA functional is included by using the DFT-D3 method of Grimme [41]. To avoid the interaction between two adjacent layers, a vacuum space of 30 Å is placed along the z direction. All atoms in the unit cell are fully relaxed until a precision of 10^{-5} eV in energy and 0.02 eV/Å in residual forces are reached. Because of the intrinsic dipole in the MoSSe system, a dipole correction in its normal direction is included throughout the calculations [42].

The nonadiabatic molecular dynamics (NAMD) simulation is calculated by the PYXAID code [43,44], which uses a decoherence-induced surface hopping technique to treat the electron-hole recombination dynamics [45]. A detailed description of the algorithm can be found in previous work [46–48]. The Janus-MoSSe bilayer is heated to 300 K, and 5 ps adiabatic molecular dynamics (MD) calculations are carried out with a 1 fs atomic time step, which yields the Hamiltonian of nonadiabatic couplings. The 5 ps nonadiabatic Hamiltonians are iterated four times to calculate the recombination dynamics over a long period. 2000 random number sequences are used to sample the surface hopping probabilities. The first 3000 geometries from the first adiabatic MD trajectories are chosen as initial conditions for the NAMD simulations.

III. RESULTS AND DISCUSSION

The structures of the untwisted (utBLM) and twisted bilayer Janus-MoSSe (tBLM) are shown in Fig. 1. From the side view, we can see that Janus-MoSSe has a sandwiched structure where the Mo plane is sandwiched between the S and Se layers. Due to the breaking of symmetry, the MoSSe monolayer has a spontaneous polarization along the z direction. Considering the different interface between two layers,

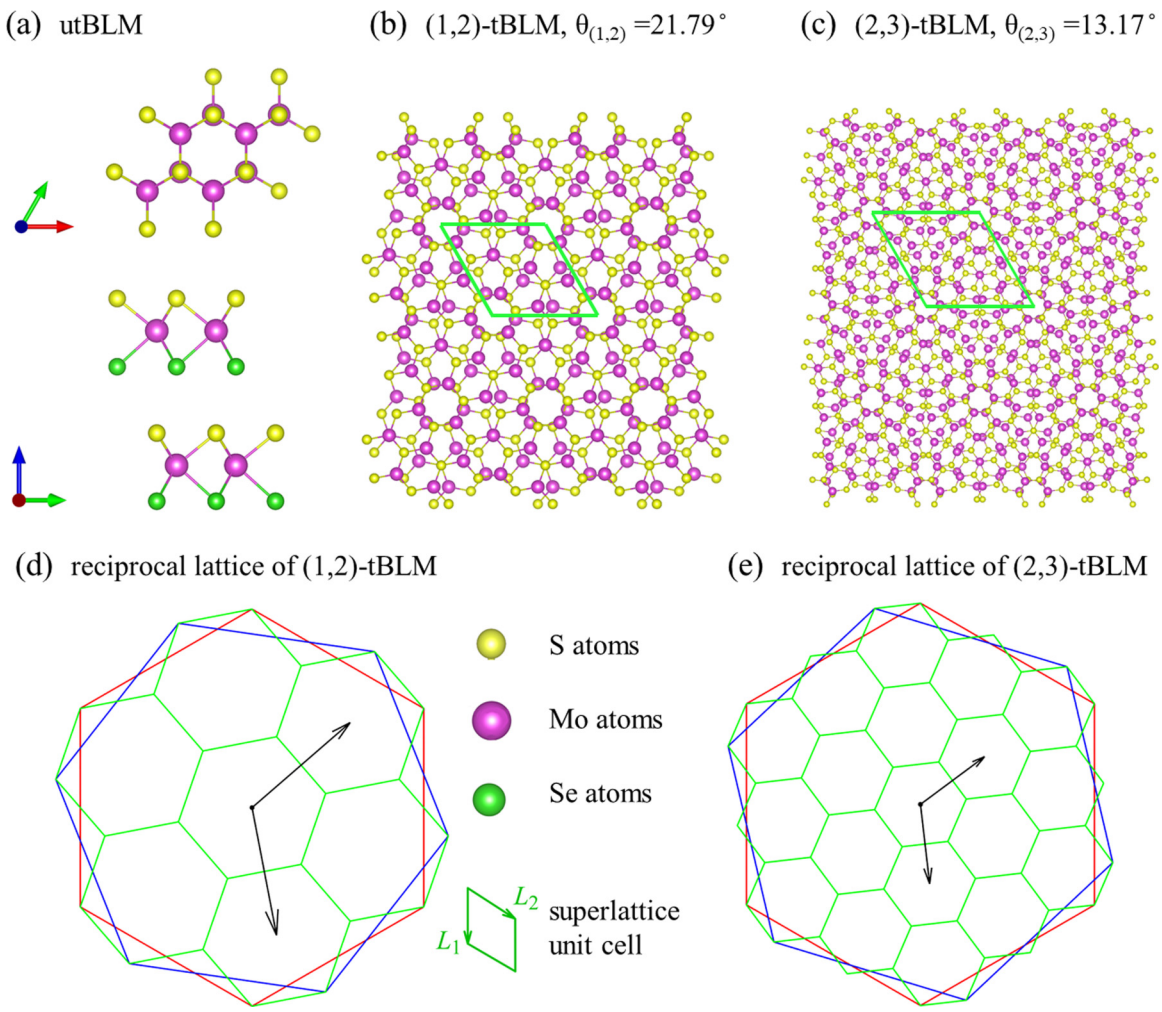

FIG. 1. (a) Top and side views of utBLM, and superlattice of (b) (1,2)-tBLM with $\theta = 21.79°$ and in (c) (2,3)-tBLM with $\theta = 13.17°$. Solid green parallelogram corresponds to the superlattice unit cell of the tBLMs. The reciprocal lattice of (d) (1,2)- and (e) (2,3)-tBLMs. The large red and blue hexagons are the first Brillouin zone of the top and bottom MoSSe layers, and the solid green hexagons represent the Wigner-Seitz cells of the reciprocal lattices corresponding to the superlattices.

the bilayer configuration of MoSSe has three types of interface, e.g., S-Se, S-S, and Se-Se. For the S-S and Se-Se interface, the MoSSe bilayer restores the symmetry, which leads to the disappearance of the built-in electric field. To maintain the intrinsic electric field, a S-Se interface type is chosen in the following research. According to the possible atom sites, there are five possible high-symmetry stacking orders. The most energetically stable stacking order is AA' (characteristic of $2H$ phase), i.e., eclipsed stacking with Mo over S (Se) atoms as demonstrated in Fig. 1(a) [49]. Thus, in the following calculations we focus on this kind of stacking configuration. The optimized lattice parameter of AA' stacking is 3.22 Å. The Mo-S and Mo-Se bond lengths are 2.42 and 2.54 Å, respectively.

To discuss the electronic properties in tBLM, we need to first analyze its crystallographic and moiré superlattices. According to previous research, the lattice structure of moiré can be represented by a pair of mutual prime numbers $(m, n)(m \neq n)$ and denoted as (m, n)-tBLM [50]. The lattice structures of the (1,2)- and (2,3)-tBLM are shown in Figs. 1(b) and 1(c). We denote the basic vectors as a_1 and a_2 for the top MoSSe layer, and a_1' and a_2' for the bottom MoSSe layer. A rigorously periodic lattice structure can be formed in some special θ, which is given by

$$\cos\theta = \frac{m^2 + 4mn + n^2}{2(m^2 + mn + n^2)}. \tag{1}$$

The lattice vectors of a unit cell in a rhombus for the tBLM can be obtained as

$$\begin{aligned} \boldsymbol{L_1} &= m\boldsymbol{a_1} + n\boldsymbol{a_2} = n\boldsymbol{a_1'} + m\boldsymbol{a_2'}, \\ \boldsymbol{L_2} &= (m+n)\boldsymbol{a_1} - n\boldsymbol{a_2} = (m+n)\boldsymbol{a_1'} + m\boldsymbol{a_2'}. \end{aligned} \tag{2}$$

Therefore, the corresponding lattice constant is written as

$$\begin{aligned} L &= |\boldsymbol{L_1}| = |\boldsymbol{L_2}| = a\sqrt{m^2 + mn + n^2} \\ &= \frac{a|m-n|}{2sin(\theta/2)}, \end{aligned} \tag{3}$$

where a is the lattice constant of the MoSSe monolayer, i.e., 3.22 Å in our case. The lattice constant for the moiré pattern can be represented by

$$L^M = \left|\boldsymbol{L_1^M}\right| = \left|\boldsymbol{L_2^M}\right| = \frac{a}{2\sin(\theta/2)}. \tag{4}$$

We can see that the unit cell of the crystallographic superlattice is identical to that of the moiré pattern when $|m-n| = 1$, while if $|m-n| \neq 1$ the former is larger than the latter. The Wigner-Seitz cell corresponding to moiré superlattices of the (1,2)- and (2,3)-tBLMs in reciprocal space are shown in Figs. 1(d) and 1(e), respectively. The large red and blue hexagons correspond to the first Brillouin zones (BZs) of the top and bottom monolayers, respectively. The reciprocal-lattice vectors of the top and bottom MoSSe layers are defined as b_1, b_2 and b_1', b_2', respectively, where the lengths of these four vectors are $b_1 = b_2 = b_1' = b_2' = b = 4\pi/\sqrt{3}a$. As shown in Figs. 1(d) and 1(e), the corresponding moiré reciprocal lattice can be defined as $g = b_1' - b_1$ and $g' = b_2 - b_2'$ with $|g| = |g'| = 2b\sin(\theta/2)$. To form the moiré pattern, a larger superlattice is needed that causes the folding of the band structure. The K^+ points of the top and bottom MoSSe layer are folded to K^+ and K^- points of tBLM, respectively, while the M and Γ points of the top and bottom MoSSe layer are folded to the M and Γ points of tBLM, respectively.

TABLE I. The calculated lattice constants a and b, interlayer distance d, direct band gaps E_g^d at the K point, and indirect band gaps E_g^i between K and Γ points.

System	Lattice constant (Å)	Distance (Å)	Band gap (eV)	
	a	d	E_g^d	E_g^i
utBLM	3.21	3.14	0.98	0.80
(1,2)-tBLM	8.60	3.31	0.99	0.85
(2,3)-tBLM	12.27	3.30	1.00	0.85

The band structures of three bilayers are plotted in Fig. 2. In agreement with previous research, a direct-to-indirect band-gap transition occurs when the number of layers increases. Due to the different orbital contributions for $K^{\pm}$ and Γ points, the energy difference between conduction and valence bands at $K^{\pm}$ points is nearly unaffected in progressing from monolayer to bilayer, while the latter is highly susceptible to the number of layers. As shown in Table I, the direct band gaps at K points of three bilayers are basically the same, whereas the indirect band gaps between K and Γ points of utBLM are slightly different. Due to the increase of interlayer distance in tBLM, the position of the valence band at the Γ point shifts down, leading to a decrease of the indirect band gap. The contributions of the top and bottom MoSSe layer are represented by red and blue lines, respectively. Different from MoS_2 or $MoSe_2$ bilayers, the Janus-MoSSe bilayer has a staggered gap where the VBM and CBM are derived from different individual layers.

Note that such type-II band alignment is robust against external perturbations, such as twisting or stacking modes, which can be attributed to the intrinsic electric field. The partial charge density of other stacking modes is given in Fig. S3 of the supplemental material [51]. Similar trends are also found for trilayer and more layers. The band structures of trilayer, four-layer, and five-layer MoSSe are demonstrated in Fig. S4. As the number of layers increases, the band gap declines rapidly and shows metallic behavior when the number of layers is greater than 4. However, the spatial separation of VBM and CBM at the K point is not impacted at all. As shown in Fig. S5, the VBM and CBM are located at the topmost and the bottom layers, suggesting that the type-II band alignment in MoSSe layers is independent of the thickness.

To better understand the influence of the intrinsic electric field on the electronic structure, we investigate the mechanism of how the built-in electric field results in the different contributions of two layers. The direction of the intrinsic electric field is from the bottom layer to the top layer, and the electrostatic potential difference $[\Delta(\Phi)]$ of the two surfaces is 1.39 eV, as seen in Fig. S1. When an excited electron leaps into the conduction band, it leaves behind a hole in the valence band. Therefore, the valence band can be considered as positively charged while the conduction band can be considered as negatively charged. As a result of an intrinsic electric field, the electron and hole move in opposite directions, leading to

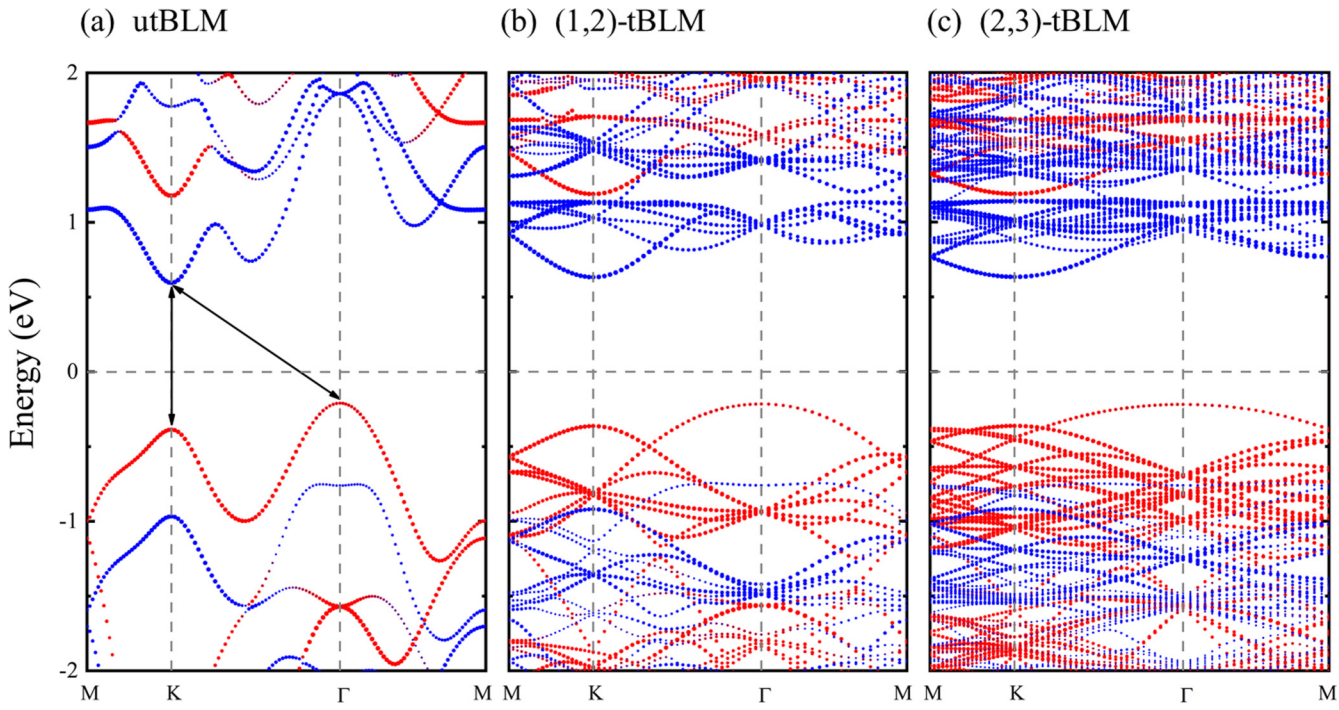

FIG. 2. The calculated component-projected energy-band structure of (a) utBLM, (b) (1,2)-tBLM, and (c) (2,3)-tBLM at the PBE level. Blue and red represent the contributions of the bottom and top MoSSe layers. The Fermi level is set to zero.

the spatial separation of valence and conduction bands. The partial charge density for the VBM and CBM of utBLM, (1,2)-, and (2,3)-tBLM at the high-symmetry point *K* is shown in Fig. 3. We can see that the VBM states are located at the Mo and S atoms of the top layer, while the CBM states stay at the Mo and Se atom of the bottom layer. On the other hand, the S and Se atoms within the interface sides of the MoSSe bilayer barely contribute to the VBM and CBM states, indicating a small wave-function overlap and hence suppression of the interlayer couplings. In Fig. S6 of the supplemental material, we also include the spin-orbital coupling (SOC) to check the possible effect on the system. Indeed, SOC results in the splitting of the valence band [see Fig. S6(a)]. However, the calculated partial charge density shows that the VBM and CBM are located at different layers. As shown in Fig. S6(b), there is only a small wave-function overlap at the interface, which suggests that the interlayer coupling is suppressed. These results are similar to those obtained without including SOC. As such, we believe that SOC does not affect the long recombination time in MoSSe bilayers.

We attribute the robustness of the type-II band alignment to the suppressed interlayer coupling, which originates from the

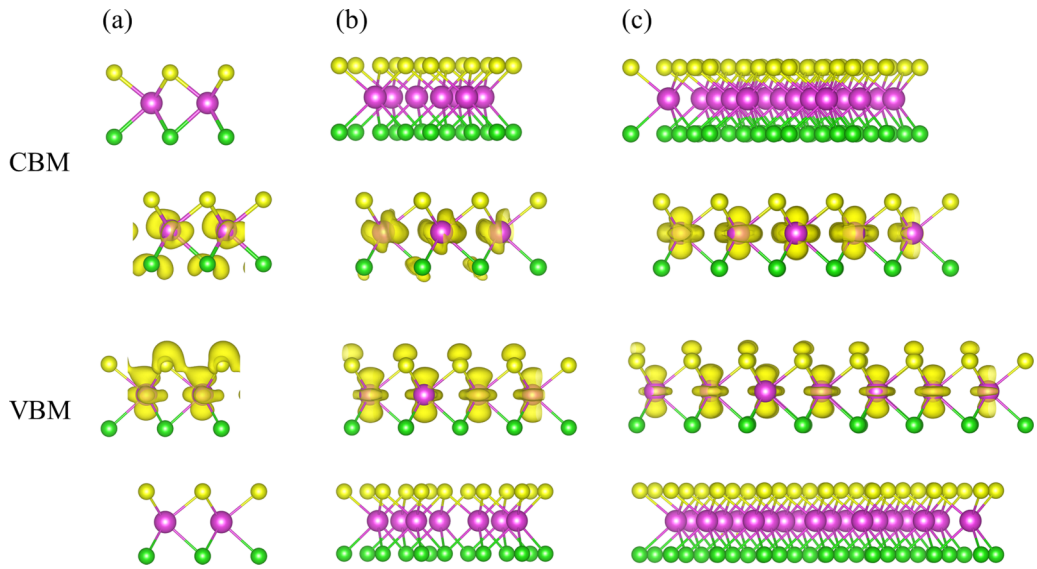

FIG. 3. The partial charge density of (a) uTBLM, (b) (1,2)-tBLM, and (c) (2,3)-tBLM at high-symmetry point *K*.

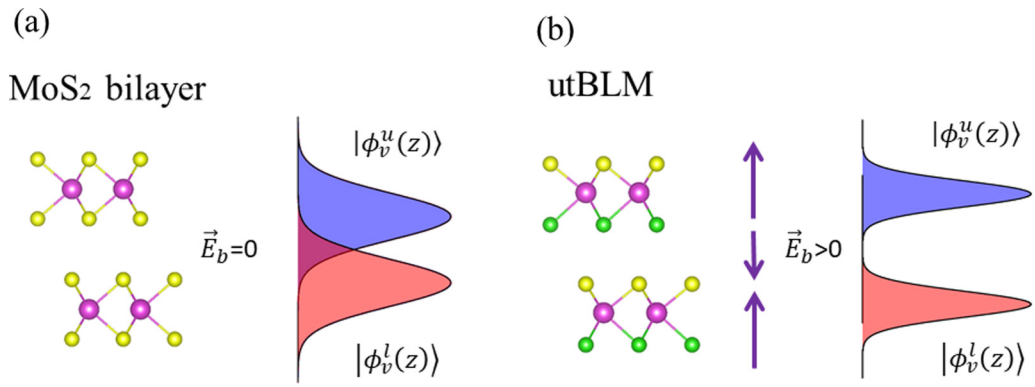

FIG. 4. Illustration of the wave-function overlap of (a) MoS_2 bilayer and (b) uTBLM. The out-of-plane wave functions of electrons in the upper-layer valence band and the one in the lower-layer valence band are represented, respectively, by envelope filling by blue and red. Their overlaps are represented by envelope filling by purple. The intra- and interlayer built-in electric fields are represented by purple arrows.

vdW force between the upper and lower layers. Because of the threefold rotating symmetry, the interlayer coupling of the conduction bands actually vanishes [52], which leads to the Hamiltonian without a built-in electric field at the K point as

$$H_K^0 = \begin{bmatrix} E_c^u & 0 & 0 & 0 \\ 0 & E_v^u & 0 & t_0 \\ 0 & 0 & E_c^l & 0 \\ 0 & t_0 & 0 & E_v^l \end{bmatrix}. \tag{5}$$

Here, the subscript $v\,(c)$ represents the valence (conduction) band, and the superscript $u\,(l)$ represents the upper (lower) layer. The built-in electric field existing in the Janus-MoSSe bilayer can be divided into two parts: the intralayer built-in electric fields in both layers and the interlayer one between the two layers. Since the direction of the built-in electric field is from Se atoms to S atoms, obviously the interlayer built-in electric field is in the opposite direction to that of the intralayer field (Fig. 4). The combination of the intra- and interlayer built-in electric fields has two major mechanisms in the suppression of the interlayer coupling. One is that the electric potentials are different in the upper and lower layers, which introduces energy level splitting. The other is that the z-direction distance between the electron in the upper-layer valence band and the one in the lower-layer valence band becomes greater, and thus the overlapping between the wave functions of electrons in the different layers greatly decreases. In this sense, the Hamiltonian with the built-in electric fields at the K point becomes

$$H_K^E = \begin{bmatrix} E_c^u - \frac{\Delta}{2} & 0 & 0 & 0 \\ 0 & E_v^u - \frac{\Delta}{2} & 0 & t \\ 0 & 0 & E_c^l + \frac{\Delta}{2} & 0 \\ 0 & t & 0 & E_v^l + \frac{\Delta}{2} \end{bmatrix}. \tag{6}$$

Here, the electric potential difference $\Delta \approx 0.58$ eV is obtained from our DFT calculation. The interlayer coupling is defined by the total Hamiltonian H between the hole wave functions in the upper and lower layers as

$$\begin{aligned} t &= \langle \phi_v^u | H | \phi_v^l \rangle \\ &\approx \langle \phi_v^u(x,y) | H | \phi_v^l(x,y) \rangle \langle \phi_v^u(z) | \phi_v^l(z) \rangle \\ &= t_0 \langle \phi_v^u(z) | \phi_v^l(z) \rangle, \end{aligned} \tag{7}$$

where we have assumed the Hamiltonian is independent of the z direction in the second step. Obviously, the built-in electric field affects the overlapping of the z-direction wave function by separating their centers. As shown in Fig. 4(a), there exist large overlapping states for the z-direction wave functions, resulting in a fast recombination rate. Nevertheless, the strong interlayer coupling can be suppressed if the centers of the z-direction wave function are sufficiently separated due to the built-in electric field [see Fig. 4(b)]. In this sense, the conduction bands have no interlayer mixing, while the valence-band interlayer mixing can be straightforwardly obtained as

$$\begin{aligned} \sin\theta &= \frac{|t|}{\sqrt{|t|^2 + \Delta^2}} \\ &= \frac{t_0 \left| \langle \phi_v^u(z) | \phi_v^l(z) \rangle \right|}{\sqrt{t_0^2 \left| \langle \phi_v^u(z) | \phi_v^l(z) \rangle \right|^2 + \Delta^2}}. \end{aligned} \tag{8}$$

If the interlayer coupling is chosen as $t_0 = 60$ meV [53] and the layer mixing is less than 0.5% obtained from our numerical calculation, the z-direction wave-function overlap can be decreased down to 4.83%.

The suppression of interlayer coupling may result in a significant improvement of the recombination time. To further investigate the electron-hole recombination kinetics, we perform the TD-DFT simulation. The nonradiative electron-hole recombination time is obtained by using the short-time linear expansion of exponential decay, i.e., $P(t) = \exp(-t/\tau) \approx 1 - t/\tau$. The results are shown in Fig. 5. Compared with previous reports, the calculated 16.5 ns recombination time of the MoSSe bilayer is one order of magnitude larger than that of its monolayer, i.e., 0.44 ns. This value is even longer than the time scales in heterostructures such as MoS_2/WS_2, MoS_2/TiO_2, and MoS_2/WSe_2. This is because in the case of monolayer MoSSe, the built-in electric field reduces the overlapping of the out-of-plane wave function, which gives rise to a weak coupling between VBM and CBM states. However, due to the restriction of the space, there is always a small overlapping at Mo atoms in the MoSSe monolayer [54]. With regard to the bilayer situation, on the other hand, the larger electrostatic potential difference and sufficient space promote the separation of out-of-plane wave-function centers, which significantly reduces the overlapping of the z-direction

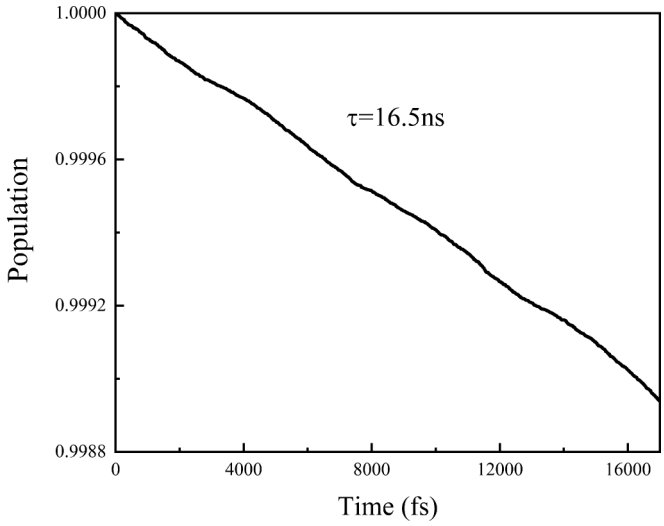

FIG. 5. Electron-hole recombination dynamics for the Janus-MoSSe bilayer.

wave functions, leading to a relatively small recombination rate. Additionally, since the type-II band alignment is robust against the twisting and stacking orders, the electron-hole wave-function overlap along the z direction of excitons should still be greatly suppressed when we alter the stacking order of the bilayer or twist the top layer to form a moiré superlattice. In this sense, the recombination time is almost independent of twisting and stacking orders. These results suggest that the Janus-MoSSe bilayer is a promising candidate for further electronic and optoelectronic applications. We should point out that despite the advanced synthetic technology, various defects and impurities are inevitable in the material, which may create electronic trap states and affect the performance. According to a previous report [55], both a sulfur adatom and a sulfur vacancy in monolayer MoS_2 can accelerate electron-hole recombination with different mechanisms. Due to the similar chemical constitution, MoSSe may be affected in the same way. To obtain the best performance, both the sulfur adatom and the vacancy should be avoided during synthesis of MoSSe.

IV. CONCLUSIONS

In summary, we systematically study the electronic properties of untwisted and twisted Janus-MoSSe bilayers by using first-principles calculation. Our results show that due to the distinction of electronegativity between S and Se atoms, Janus-MoSSe exhibits a vertical intrinsic electric field. In the case of a MoSSe bilayer, the existence of a built-in electric field promotes the spatial separation of VBM and CBM states and leads to a robust type-II band alignment. The electron-hole recombination time is evaluated in the framework of the NAMD technique. The predicted lifetime is up to 16.5 ns, which is even longer than that of the MoS_2/WS_2 vdW heterostructure. The extremely long timescale for electron-hole recombination can be interpreted by the reduction of the out-of-plane wave functions overlapping between VBM and CBM states and the completely spacial separation between electron and hole. From all the above, we propose that introducing an intrinsic electric field can significantly extend the recombination time of a photoexcited electron and hole, and thus provide a promising approach to engineer the electronic and optical properties in a vdW bilayer for further optoelectronic and valleytronic applications.

ACKNOWLEDGMENTS

This work is supported by the National Natural Science foundation of China (No. 11604213 and No. 21333006), the Taishan Scholar Program of Shandong Provice, 111 Project (B13029), and Shenzhen Key Lab Fund (Grant No. ZDSYS20170228105421966).

[1] K. S. Novoselov, A. K. Geim, S. V. Morozov, D. Jiang, Y. Zhang, S. V. Dubonos, I. V. Grigorieva, and A. A. Firsov, Science **306**, 666 (2004).
[2] S. Stankovich, D. A. Dikin, R. D. Piner, K. A. Kohlhaas, A. Kleinhammes, Y. Jia, Y. Wu, S. T. Nguyen, and R. S. Ruoff, Carbon **45**, 1558 (2007).
[3] Y. Hernandez, V. Nicolosi, M. Lotya, F. M. Blighe, Z. Sun, S. De, I. T. McGovern, B. Holland, M. Byrne, Y. K. Gun'Ko, J. J. Boland, P. Niraj, G. Duesberg, S. Krishnamurthy, R. Goodhue, J. Hutchison, V. Scardaci, A. C. Ferrari, and J. N. Coleman, Nat. Nanotechnol. **3**, 563 (2008).
[4] L. Li, Y. Yu, G. J. Ye, Q. Ge, X. Ou, H. Wu, D. Feng, X. H. Chen, and Y. Zhang, Nat. Nanotechnol. **9**, 372 (2014).
[5] H. Liu, A. T. Neal, Z. Zhu, Z. Luo, X. Xu, D. Tománek, and P. D. Ye, ACS Nano **8**, 4033 (2014).
[6] C. Zhi, Y. Bando, C. Tang, H. Kuwahara, and D. Golberg, Adv. Mater. **21**, 2889 (2009).
[7] S. Z. Butler, S. M. Hollen, L. Cao, Y. Cui, J. A. Gupta, H. R. Gutiérrez, T. F. Heinz, S. S. Hong, J. Huang, A. F. Ismach, E. Johnston-Halperin, M. Kuno, V. V. Plashnitsa, R. D. Robinson, R. S. Ruoff, S. Salahuddin, J. Shan, L. Shi, M. G. Spencer, M. Terrones, W. Windl, and J. E. Goldberger, ACS Nano **7**, 2898 (2013).
[8] M. Xu, T. Liang, M. Shi, and H. Chen, Chem. Rev. **113**, 3766 (2013).
[9] A. Kuc and T. Heine, Chem. Soc. Rev. **44**, 2603 (2015).
[10] R. Peng, Y. Ma, Z. He, B. Huang, L. Kou, and Y. Dai, Nano Lett. **19**, 1227 (2019).
[11] Q. Sun, Y. Dai, Y. Ma, T. Jing, W. Wei, and B. Huang, J. Phys. Chem. Lett. **7**, 937 (2016).
[12] R. Peng, Y. Ma, B. Huang, and Y. Dai, J. Mater. Chem. A **7**, 603 (2019).
[13] A. K. Geim and I. V. Grigorieva, Nature (London) **499**, 419 (2013).
[14] K. S. Novoselov, A. Mishchenko, A. Carvalho, and A. H. Castro Neto, Science **353**, aac9439 (2016).

[15] Y. Liu, N. O. Weiss, X. Duan, H.-C. Cheng, Y. Huang, and X. Duan, Nat. Rev. Mater. **1**, 16042 (2016).

[16] M. Yagmurcukardes, E. Torun, R. T. Senger, F. M. Peeters, and H. Sahin, Phys. Rev. B **94**, 195403 (2016).

[17] S. Bettis Homan, V. K. Sangwan, I. Balla, H. Bergeron, E. A. Weiss, and M. C. Hersam, Nano Lett. **17**, 164 (2017).

[18] P. Rivera, K. L. Seyler, H. Yu, J. R. Schaibley, J. Yan, D. G. Mandrus, W. Yao, and X. Xu, Science **351**, 688 (2016).

[19] B. Miller, A. Steinhoff, B. Pano, J. Klein, F. Jahnke, A. Holleitner, and U. Wurstbauer, Nano Lett. **17**, 5229 (2017).

[20] P. Rivera, J. R. Schaibley, A. M. Jones, J. S. Ross, S. Wu, G. Aivazian, P. Klement, K. Seyler, G. Clark, N. J. Ghimire, J. Yan, D. G. Mandrus, W. Yao, and X. Xu, Nat. Commun. **6**, 6242 (2015).

[21] C. Long, Z.-R. Gong, H. Jin, and Y. Dai, J. Phys.: Condens. Matter **30**, 395001 (2018).

[22] Y. Wang, Z. Wang, W. Yao, G.-B. Liu, and H. Yu, Phys. Rev. B **95**, 115429 (2017).

[23] K. F. Mak and J. Shan, Nat. Nanotechnol. **13**, 974 (2018).

[24] Y. Li, Q. Cui, F. Ceballos, S. D. Lane, Z. Qi, and H. Zhao, Nano Lett. **17**, 6661 (2017).

[25] A.-Y. Lu, H. Zhu, J. Xiao, C.-P. Chuu, Y. Han, M.-H. Chiu, C.-C. Cheng, C.-W. Yang, K.-H. Wei, Y. Yang, Y. Wang, D. Sokaras, D. Nordlund, P. Yang, D. A. Muller, M.-Y. Chou, X. Zhang, and L.-J. Li, Nat. Nanotechnol. **12**, 744 (2017).

[26] L. Dong, J. Lou, and V. B. Shenoy, ACS Nano **11**, 8242 (2017).

[27] R. K. Defo, S. Fang, S. N. Shirodkar, G. A. Tritsaris, A. Dimoulas, and E. Kaxiras, Phys. Rev. B **94**, 155310 (2016).

[28] Q.-F. Yao, J. Cai, W.-Y. Tong, S.-J. Gong, J.-Q. Wang, X. Wan, C.-G. Duan, and J. H. Chu, Phys. Rev. B **95**, 165401 (2017).

[29] F. Li, W. Wei, P. Zhao, B. Huang, and Y. Dai, J. Phys. Chem. Lett. **8**, 5959 (2017).

[30] W.-J. Yin, B. Wen, G.-Z. Nie, X.-L. Wei, and L.-M. Liu, J. Mater. Chem. C **6**, 1693 (2018).

[31] X. Ma, X. Wu, H. Wang, and Y. Wang, J. Mater. Chem. A **6**, 2295 (2018).

[32] T. Hu, F. Jia, G. Zhao, J. Wu, A. Stroppa, and W. Ren, Phys. Rev. B **97**, 235404 (2018).

[33] Y. Wei, L. Li, W. Fang, R. Long, and O. V. Prezhdo, Nano Lett. **17**, 4038 (2017).

[34] L. Li, R. Long, and O. V. Prezhdo, Chem. Mater. **29**, 2466 (2017).

[35] Y. Yang, W.-H. Fang, and R. Long, J. Phys. Chem. Lett. **8**, 5771 (2017).

[36] G. Kresse and D. Joubert, Phys. Rev. B **59**, 1758 (1999).

[37] P. E. Blöchl, Phys. Rev. B **50**, 17953 (1994).

[38] G. Kresse and J. Furthmüller, Comput. Mater. Sci. **6**, 15 (1996).

[39] G. Kresse and J. Furthmüller, Phys. Rev. B **54**, 11169 (1996).

[40] J. P. Perdew, K. Burke, and M. Ernzerhof, Phys. Rev. Lett. **77**, 3865 (1996).

[41] S. Grimme, J. Antony, S. Ehrlich, and H. Krieg, J. Chem. Phys. **132**, 154104 (2010).

[42] J. Neugebauer and M. Scheffler, Phys. Rev. B **46**, 16067 (1992).

[43] A. V. Akimov and O. V. Prezhdo, J. Chem. Theory Comput. **9**, 4959 (2013).

[44] A. V. Akimov and O. V. Prezhdo, J. Chem. Theory Comput. **10**, 789 (2014).

[45] H. M. Jaeger, S. Fischer, and O. V. Prezhdo, J. Chem. Phys. **137**, 22A545 (2012).

[46] C. F. Craig, W. R. Duncan, and O. V. Prezhdo, Phys. Rev. Lett. **95**, 163001 (2005).

[47] T. R. Nelson and O. V. Prezhdo, J. Am. Chem. Soc. **135**, 3702 (2013).

[48] S. A. Fischer, W. R. Duncan, and O. V. Prezhdo, J. Am. Chem. Soc. **131**, 15483 (2009).

[49] J. He, K. Hummer, and C. Franchini, Phys. Rev. B **89**, 075409 (2014).

[50] M.-L. Lin, Q.-H. Tan, J.-B. Wu, X.-S. Chen, J.-H. Wang, Y.-H. Pan, X. Zhang, X. Cong, J. Zhang, W. Ji, P.-A. Hu, K.-H. Liu, and P.-H. Tan, ACS Nano **12**, 8770 (2018).

[51] See Supplemental Material at http://link.aps.org/supplemental/10.1103/PhysRevB.99.115316 for the electronic properties of MoS_2, different stacking MoSSe bilayers, multilayer MoSSe, and the AA' stacking MoSSe bilayer with spin-orbit interaction correction.

[52] Z. Gong, G.-B. Liu, H. Yu, D. Xiao, X. Cui, X. Xu, and W. Yao, Nat. Commun. **4**, 2053 (2013).

[53] H. Rydberg, M. Dion, N. Jacobson, E. Schröder, P. Hyldgaard, S. I. Simak, D. C. Langreth, and B. I. Lundqvist, Phys. Rev. Lett. **91**, 126402 (2003).

[54] H. Jin, T. Wang, Z.-R. Gong, C. Long, and Y. Dai, Nanoscale **10**, 19310 (2018).

[55] L. Li, R. Long, T. Bertolini, and O. V. Prezhdo, Nano Lett. **17**, 7962 (2017).